

## X-ray Studies of the Inverted Ejecta Layers in the Southeast Area of Cassiopeia A

TOMOYA TSUCHIOKA <sup>1</sup>, TOSHIKI SATO <sup>1</sup>, SHINYA YAMADA <sup>1</sup> AND YASUNOBU UCHIYAMA<sup>1</sup>

<sup>1</sup>*Department of Physics, Rikkyo University, 3-34-1 Nishi Ikebukuro, Toshima-ku, Tokyo 171-8501, Japan*

Submitted to ApJ

### ABSTRACT

The central strong activities in core-collapse supernovae expect to produce the overturning of the Fe- and Si/O-rich ejecta during the supernova explosion based on multi-dimensional simulations. X-ray observations of the supernova remnant Cassiopeia A have indicated that the Fe-rich ejecta lies outside the Si-rich materials in the southeastern region, which is consistent with the hypothesis on the inversion of the ejecta. We investigate the kinematic and nucleosynthetic properties of the inverted ejecta layers in detail to understand its formation process using the data taken by the Chandra X-ray Observatory. Three-dimensional velocities of Fe- and Si/O-rich ejecta are obtained as  $>4,500$  km s<sup>-1</sup> and  $\sim 2,000$ – $3,000$  km s<sup>-1</sup>, respectively, by combining proper motion and line-of-sight velocities, indicating that the velocity of the Si/O-rich ejecta is slower than that of the Fe-rich ejecta since the early stage of the explosion. To constrain their burning regime, the Cr/Fe mass ratios are evaluated as  $0.51^{+0.11}_{-0.10}\%$  in the outermost Fe-rich region and  $1.24^{+0.19}_{-0.20}\%$  in the inner Fe/Si-rich region, suggesting that the complete Si burning layer is invertedly located to the incomplete Si burning layer. All the results support the ejecta overturning at the early stages of the remnant's evolution or during the supernova explosion of Cassiopeia A.

*Keywords:* ISM: individual objects (SNR Cassiopeia A) – ISM: supernova remnants – proper motions – nucleosynthesis

### 1. INTRODUCTION

Stars with masses higher than about  $8 M_{\odot}$  undergo a gravitational core-collapse supernova (CC SN) explosion at the final stage of their evolution. Currently, the explosion mechanism of CC SNe is one of the unsolved problems in astrophysics. In theory, central asymmetric effects during the explosion are widely believed to help such massive stars to explode (e.g., Burrows et al. 1995; Janka & Mueller 1996; Khokhlov et al. 1999; Fryer & Heger 2000; Blondin et al. 2003; Takiwaki et al. 2009, 2012; Janka 2012; Janka et al. 2016; Burrows & Vartanyan 2021). However, it is difficult to investigate the asymmetric mechanisms only from SN observations.

Observations of supernova remnants (SNRs) provide us a great opportunity to examine those asymmetries during SN explosions. Especially in young SNRs, the distribution of synthesized elements and their kinemat-

ics provide us unique information on the asymmetries at the explosion, such as neutrino-star kick, ejecta mixing, and so on (e.g., Winkler & Petre 2007; Lopez et al. 2011, 2013; Holland-Ashford et al. 2017; Katsuda et al. 2018; Holland-Ashford et al. 2020; Picquenot et al. 2021; Tsuchioka et al. 2021; Sato et al. 2021). Here, the galactic supernova remnant Cassiopeia A (Cas A) is one of the most well-studied samples to discuss it. The highly asymmetric ejecta distributions of the remnant were observed in detail at multiple wavelengths (e.g., Fesen et al. 2001, 2006; Smith et al. 2009; DeLaney et al. 2010; Isensee et al. 2010; Grefenstette et al. 2014; Isensee et al. 2012; DeLaney et al. 2014; Alarie et al. 2014; Patnaude & Fesen 2014; Milisavljevic & Fesen 2015; Fesen & Milisavljevic 2016; Grefenstette et al. 2017; Ikeda et al. 2022), which can be a unique tool to test the asymmetric effects by comparing them with theoretical calculations (e.g., Schure et al. 2008; Wheeler et al. 2008; Orlando et al. 2016; Wongwathanarat et al. 2017; Orlando et al. 2021).

One of the peculiar structures observed in Cassiopeia A would be the Fe-rich ejecta located at the tip of the southeastern region (Hughes et al. 2000; Hwang et al. 2000; Hwang & Laming 2003; Vink 2004; Sato et al. 2021). In general, the Fe-rich materials are synthesized at the innermost region of the SN explosions via explosive Si burning (e.g., Woosley et al. 1973; Thielemann et al. 1996).

On the other hand, the Fe-rich ejecta in the remnant is located outside of the other lighter elements such as Si and O in the 2D projected image, suggesting that some strong central activities pushed this structure outward (e.g., Hughes et al. 2000; Sato et al. 2021). For example, it has been theoretically suggested that explosions driven by bipolar jets could produce such “overturning” of the ejecta layers (e.g., Maeda & Nomoto 2003). Also, recent multi-dimensional SN simulations have indicated that the neutrino-driven mechanism can reproduce well the large clumps of the Fe-rich ejecta observed in the remnant (Wongwathanarat et al. 2017). Thus, this peculiar feature is possibly related to the central mechanism of the explosion.

While the observational and theoretical studies have supported that the inverted layers are the result of the central strong activities during the explosion, our understanding of the process of the spatial inversion is still being updated. DeLaney et al. (2010) have constructed a comprehensive 3D model of the remnant using infrared and X-ray Doppler velocity measurements, which dismissed the overturning during the explosion as the origin of the southeastern Fe-rich structures (see also Milisavljevic & Fesen 2013). The authors have proposed that “pistons” of faster than average ejecta can explain well that the Fe-rich ejecta in this region occupies a “ring” of the Si-rich ejecta. In this picture, emissions from the piston itself fade gradually after the reverse-shock passage leaving such a ring-like structure, and then the ejecta layers may remain intact or the piston may “breakthrough” the outer layers. This could have produced the observed structures where the Fe is located at the tip of the southeastern region even without the inversion of between Fe and Si layers at the explosion. Recent 3D SNR simulations (Orlando et al. 2016, 2021) have demonstrated that the Fe-rich plumes that were created during the initial stages of the SN explosion can reproduce the inverted ejecta layers in the remnant, where a similar way to the pistons seems to work during the SNR evolution for producing the spatial inversion of the ejecta layers at the age of the remnant.

In this paper, we aim to investigate both kinematic and nucleosynthetic properties of the inverted ejecta layers to understand its formation process in more detail

using X-ray observations of Cas A. From proper motion and Doppler velocity measurements, we can quantitatively assess the current 3D velocity and deceleration of each ejecta layer, which would allow us to discuss the initial kinematics of each component at the explosion. Also, with the constraints of the burning regime of each ejecta layer, we can discuss the inversion process from a different perspective than the kinematic properties. The previous observations have not reported the existence of ejecta from the incomplete Si burning layer. This would be a notable point because the incomplete Si burning layer must be located just above the complete Si burning layer in spherically symmetric SN models (e.g., Woosley & Weaver 1995; Thielemann et al. 1996). On the other hand, we can see only the products from the complete Si burning (i.e.,  $\alpha$ -rich freeze out) regime at the tip of the southeastern Fe-rich structures (e.g., Hwang & Laming 2003; Sato et al. 2021). It would be possible that the strong asymmetric activities during the explosion caused this missing layer to be located behind the complete Si burning layer (e.g., Maeda & Nomoto 2003), but it needs to be verified with observations. In particular, the inversion of these innermost layers may reflect the overturning at a very early stage of the SN/SNR evolution (at least, earlier than the inversion of the Fe/Si layers). Thus, we also aim to search for the missing incomplete Si burning layer in the southeastern region in this study.

This paper is organized as follows. The next section summarizes the observations used and the data reduction procedures applied to the data. In Section 3, we present our imaging and spectroscopic analysis of the data and results in the inverted layers of Cas A. The discussion section (Section 4) studies the kinematics and nucleosynthetic properties of the inverted layers and the final section summarizes the article. Throughout this article, uncertainties are quoted at the 90% confidence level, unless explicitly stated otherwise.

## 2. OBSERVATIONS

The Advanced CCD Imaging Spectrometer (ACIS) of Chandra has observed Cas A multiple times since its launch in 1999 (e.g., Hughes et al. 2000; Hwang et al. 2000; Patnaude & Fesen 2014; Sato et al. 2018). The observational data used in this study are summarized in Table 1. In the image analysis, we used ACIS data observed in 2000 (PI: Holt, S) and 2019 (PI: Patnaude, D). For the spectral analysis, we used data from 2004 (PI: Hwang, U) for a total of  $\sim 1$  Ms (e.g., Hwang et al. 2004). We used `merge_obs` to combine the observations of the nine ObsIDs in 2004.

We reprocessed the data using `chandra_repro` in CIAO 4.13 with CALDB 4.9.5. Before performing the

**Table 1.** Basic information on the Chandra observations of Cas A used in the analysis.

Obs. ID	Obs. Start (yyyy mm dd)	Exposure (ks)	Detector	RA (deg)	Dec (deg)	Roll (deg)
114	2000 Jan 30	49.9	ACIS-S	350.9159	58.7926	323.3801
4634	2004 Apr 28	148.6	ACIS-S	350.9047	58.8455	59.2239
4635	2004 May 1	135.0	ACIS-S	350.9048	58.8455	59.2237
4636	2004 Apr 20	143.5	ACIS-S	350.9129	58.8412	49.7698
4637	2004 Apr 22	163.5	ACIS-S	350.9131	58.8414	49.7665
4638	2004 Apr 14	164.5	ACIS-S	350.9196	58.8365	40.3327
4639	2004 Apr 25	79.0	ACIS-S	350.9132	58.8415	49.7666
5196	2004 Feb 8	49.5	ACIS-S	350.9129	58.7933	325.5035
5319	2004 Apr 18	42.3	ACIS-S	325.5035	58.8411	49.7698
5320	2004 May 5	54.4	ACIS-S	350.8988	58.8480	65.1350
19606	2019 May 13	37.6	ACIS-S	350.8854	58.8559	75.1398

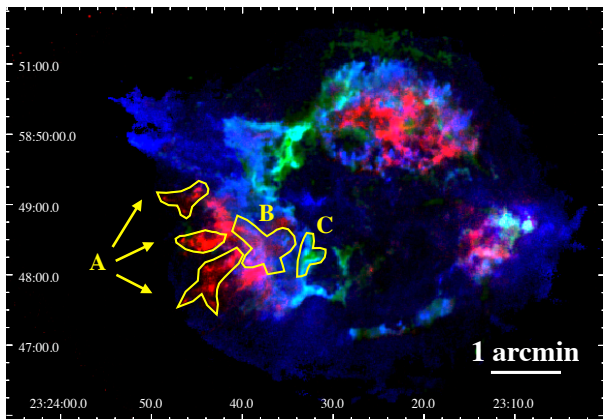
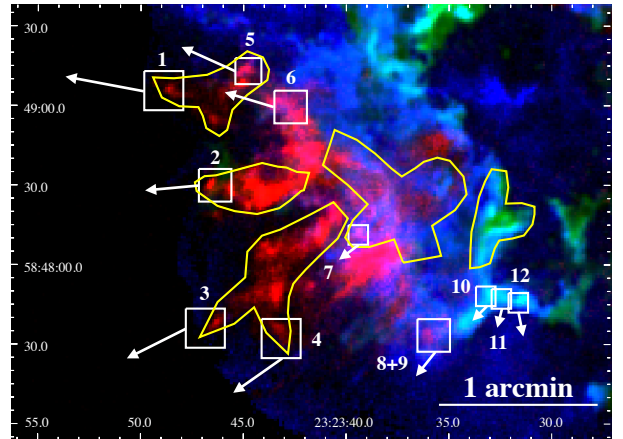
**Figure 1.** X-ray image of Cas A taken by Chandra. The red and blue colors highlight Fe-rich (6.3-6.9 keV) and O-rich (0.5-0.7 keV/0.9-1.0 keV) emission regions, respectively. The ratio map of the Si/Mg band (1.8-2.1 keV/1.2-1.6 keV) is shown in green color. Solid yellow contours show the regions used for the spectral analysis.

image analysis, we aligned the two sets of data using the coordinates of the Central Compact Object (CCO). It is the only available common point source in the two images. The coordinates of the CCO of each image were obtained with `wavdetect`, and then the position offsets were computed with `wcs.match`. Using this offset value, we recreated the image to be used for image analysis by updating the coordinates of the event file with `wcs.update`.

### 3. RESULTS

The asymmetric distribution of elements in Cas A can be seen in the intensity maps of X-ray lines from the

**Figure 2.** Enlarged image of the southeast area of Cas A. The color scheme is the same as in Figure 1. White boxes show the regions used for the proper motion analysis. White arrows indicate the direction and magnitude of the proper motion.

shocked ejecta. Figure 1 shows X-ray images of Cas A, where the Fe-rich, O-rich, and Si-rich ejecta are highlighted in red, green, and blue, respectively. In the southeastern region, we can see the inverted ejecta layers reported in the previous studies (e.g., [Hughes et al. 2000](#); [Hwang et al. 2000](#); [Vink 2004](#)), where we defined the Fe-rich, Fe/Si-rich, and Si/O-rich regions as region A, B, and C, respectively (Figure 1). In this section, we attempt two types of analysis: (1) image analysis for determining the kinematic properties (i.e., proper motions) of the ejecta and (2) spectral analysis for measuring the elemental composition to constrain the burning regime of each ejecta layer.

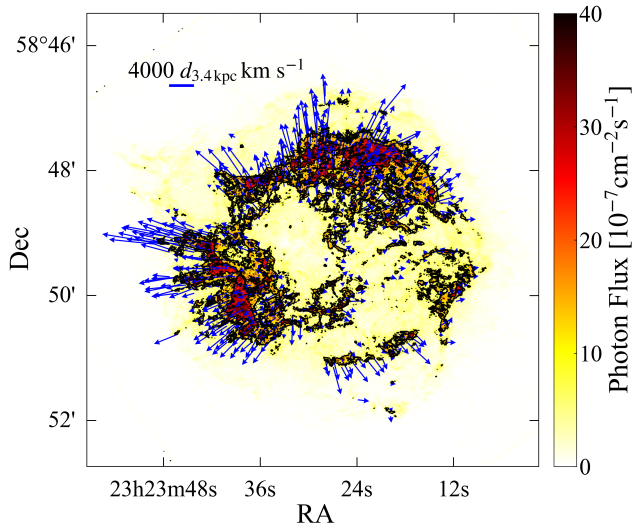


**Figure 3.** The X-ray image of Cas A in 0.5–1.7 keV observed in 2000 overlaid with the velocity vectors obtained by optical flow. The scale bar indicates the 2D space velocity of 4,000 km s<sup>-1</sup> at the distance of 3.4 kpc.

### 3.1. Proper motion measurements

We measure the proper motions of the Fe-rich and Si/O-rich ejecta in the southeastern region using some techniques to evaluate their kinematics in detail. Here we used X-ray images in the 0.5–1.7 keV band, which includes the Fe-L and O emissions, taken in 2000 and 2019.

To visualize expansions of local structures in Cas A, we used a technique called “optical flow” (Farnebäck 2003), which has been firstly applied to the remnant in Sato et al. (2018). We used the `calcOpticalFlowFarneback` function in OpenCV with the following arguments: `pyr_scale = 0.5`, which specifies the image scale to build pyramids for each image; `levels = 3`; the number of pyramid layers; `winsize = 15`; averaging window size; and `poly_n = 5`, which is the size of the pixel neighborhood used for the polynomial approximation. Assuming the distance of 3.4 kpc (Reed et al. 1995), the velocity vectors were calculated as shown in Figure 3. The moving structures at outer regions of the remnant have higher velocities, where the tip of the southeast region shows the velocities of  $> 6,000$  km s<sup>-1</sup>.

We also measured the proper motions of 11 blob regions shown in Figure 2 using the maximum likelihood method (e.g., Sato & Hughes 2017; Sato et al. 2018; Tsuchioka et al. 2021) to obtain the directions and magnitudes of the motions of each structure. Blob 5–12 in Figure 2 show the regions where the Doppler velocity measurements using High Energy Transmission Grating Spectrometer (HETGS) were performed in Rutherford

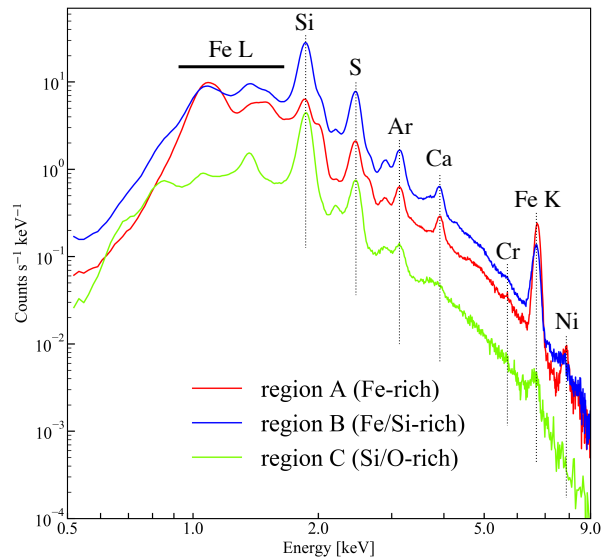


**Figure 4.** The Chandra spectra of Cas A in 0.5–9.0 keV extracted from the regions defined in Figure 1 (red: region A, blue: region B, green: region C).

et al. (2013). The regions from Blob 1 to Blob 4 were defined as the outermost regions where Fe is abundant. As a result, the best-fit velocities in the plane of the sky (see 3rd and 4th rows in Table 2) were estimated to be  $\sim 4,000$ – $7,000$  km s<sup>-1</sup> for the Fe-rich structures (Blob 1–6),  $\sim 2,000$ – $3,000$  km s<sup>-1</sup> for the Fe/Si-rich structures (Blob 7–9), and  $\sim 1,500$ – $2,500$  km s<sup>-1</sup> for the Si/O-rich structures (Blobs 10–12). The estimated velocities agree with those with the optical flow measurements. We found that the velocities of the Fe-rich structures in the plan of the sky are higher than those of the Si/O-rich structures. Even if we considered the line-of-sight (LoS) velocities obtained in Rutherford et al. (2013), the velocities of the Fe-rich structures are higher than those of the Si/O-rich structures (see 5th and 6th rows in Table 2). On the other hand, the expansion index:  $m$  ( $r \propto t^m$ , where  $r$  and  $t$  are the radius and age of the remnant, respectively) in the Si/O-rich structures estimated from the proper motion measurements are lower than that in the Fe-rich structures, which means that the Si/O-rich structures were subjected to stronger deceleration. In section 4.1, we discuss the deceleration in more detail.

### 3.2. Spectral Analysis

In Figure 4, we showed X-ray spectra extracted from region A (Fe-rich region), B (Fe/Si-rich region), and C (Si/O-rich region). The comparison of the spectra shows that abundant elements are different from region to region, where elements that are prominent in the image appear as strong features in the spectra. We here focus on that the Si/Fe-rich structure (region B) is located

**Table 2.** Velocity measurements in the regions shown in Figure 2 from Chandra data

Region <sup>a</sup>	(R.A., Decl.)	Angular velocity		LoS velocity <sup>c</sup>	Total	Expansion index, $m^d$	Free expansion velocity <sup>d</sup>
		(arcsec yr <sup>-1</sup> )	(km s <sup>-1</sup> ) <sup>b</sup>	(km s <sup>-1</sup> )	(km s <sup>-1</sup> )		(km s <sup>-1</sup> )
Blob 1	23 <sup>h</sup> 23 <sup>m</sup> 48. <sup>s</sup> 89, 58°49′05. <sup>″</sup> 59	0.415 ± 0.026	6700 ± 410	-	-	0.859 ± 0.053	7790
Blob 2	23 <sup>h</sup> 23 <sup>m</sup> 46. <sup>s</sup> 38, 58°48′29. <sup>″</sup> 94	0.282 ± 0.026	4540 ± 410	-	-	0.666 ± 0.060	6820
Blob 3	23 <sup>h</sup> 23 <sup>m</sup> 46. <sup>s</sup> 85, 58°47′36. <sup>″</sup> 06	0.342 ± 0.026	5520 ± 410	-	-	0.722 ± 0.054	7640
Blob 4	23 <sup>h</sup> 23 <sup>m</sup> 43. <sup>s</sup> 16, 58°47′32. <sup>″</sup> 19	0.311 ± 0.026	5020 ± 410	-	-	0.769 ± 0.063	6520
Blob 5	23 <sup>h</sup> 23 <sup>m</sup> 44. <sup>s</sup> 77, 58°49′13. <sup>″</sup> 00	0.308 ± 0.026	4970 ± 410	-1710	5260	0.781 ± 0.065	6370
Blob 6	23 <sup>h</sup> 23 <sup>m</sup> 42. <sup>s</sup> 71, 58°48′59. <sup>″</sup> 48	0.266 ± 0.026	4290 ± 410	-1360	4500	0.781 ± 0.075	5500
Blob 7	23 <sup>h</sup> 23 <sup>m</sup> 39. <sup>s</sup> 41, 58°48′11. <sup>″</sup> 28	0.128 ± 0.026	2060 ± 410	-540	2130	0.460 ± 0.092	4480
Blob 8	23 <sup>h</sup> 23 <sup>m</sup> 35. <sup>s</sup> 74, 58°47′33. <sup>″</sup> 40	0.163 ± 0.026	2630 ± 410	-880	2780	0.607 ± 0.095	4340
Blob 9	23 <sup>h</sup> 23 <sup>m</sup> 35. <sup>s</sup> 74, 58°47′33. <sup>″</sup> 40	0.163 ± 0.026	2630 ± 410	-810	2750	0.607 ± 0.095	4340
Blob 10	23 <sup>h</sup> 23 <sup>m</sup> 33. <sup>s</sup> 21, 58°47′48. <sup>″</sup> 17	0.108 ± 0.026	1750 ± 410	-2340	2920	0.542 ± 0.128	3220
Blob 11	23 <sup>h</sup> 23 <sup>m</sup> 32. <sup>s</sup> 45, 58°47′47. <sup>″</sup> 18	0.105 ± 0.026	1700 ± 410	-2300	2860	0.548 ± 0.133	3100
Blob 12	23 <sup>h</sup> 23 <sup>m</sup> 31. <sup>s</sup> 62, 58°47′45. <sup>″</sup> 71	0.130 ± 0.026	2100 ± 410	-1360	2500	0.698 ± 0.137	3010

All errors listed in the table represent statistical errors.

<sup>a</sup>See Figure 2 for the regions. Each feature corresponds to the three regions in Figure 1: Blob 1-6 correspond to region A (Fe-rich), Blob 7-9 to region B (Fe/Si-rich), and Blob 10-12 to region C (Si/O-rich).

<sup>b</sup>The distance to Cas A is assumed to be 3.4 kpc (Reed et al. 1995).

<sup>c</sup>The LoS velocities were measured with Chandra HETG in Rutherford et al. (2013).

<sup>d</sup>Only the values of Angular velocity were used.

just inside the Fe-rich structure (region A). In general, Si/Fe-rich ejecta (i.e., the production in the incomplete Si burning layer) should be produced at the outside of Fe-rich ejecta (i.e., the production in the complete Si burning layer) in the SN explosion. Therefore, the positional relationship between region A and region B may indicate an inversion, which has not been reported yet.

To demonstrate the inversion between the complete and incomplete Si burning layers, we measured the abundances of Cr and Fe in region A and B by fitting the spectra in 3.7–7.1 keV. Since the magnitude of the Cr/Fe ratio changes between complete Si burning regime and incomplete Si burning regime (e.g., Yamaguchi et al. 2017; Sato et al. 2020a, 2021), we chose Cr and Fe to quantify their mass ratio and identify the Si burning regime. The spectra were fitted with `tbabs`, a model for interstellar absorption, and `vvpshock`, a non-equilibrium ionized plasma model. We also used a `gsmooth` model for expressing the thermal broadening and the Doppler effects. As a result, we found that the Cr/Fe mass ratio in region B is significantly higher than that in region A (Figure 5 & Table 3), which implies that they were synthesized in different burning regimes (see section 4.2 for a detailed discussion). The best-fit

parameters and the significance of the Cr detection are summarized in Table 3.

In the spectral analysis, the hydrogen column density was fixed to  $1.2 \times 10^{22} \text{ cm}^{-2}$ , which is a typical value for the southeast region (Hwang & Laming (2003); Sato et al. (2021); Ikeda et al. (2022)), while  $kT_e$ ,  $n_{e,t}$ , and normalization and abundances of Ca, Ti, Cr, Mn, and Fe are treated as free parameters and the other abundances of elements are frozen to the solar values in Anders & Grevesse (1989). In region B, we found that the spectrum has significant contributions from pileup events due to the strong Si/S He $\alpha$  emissions (see the broken lines in the bottom panels in Figure 5). Therefore, we here added two Gaussian components (`gauss` in XSPEC) at  $\sim 4.3$  keV (Si He $\alpha$  + S He $\alpha$ ) and  $\sim 4.9$  keV (S He $\alpha$   $\times$  2 or Si He $\alpha$  + Ar He $\alpha$ ) to express the line features from the pileup effect. The pileup effect would rarely affect our measurements of Cr and Fe abundances because line structures due to the pileup are expected to be too weak around these emission lines. Also, we added a Gaussian component at  $\sim 6.5$  keV to obtain a better fit for the Fe K $\alpha$  emission in region B. One possible reason for the failure to reproduce the Fe K $\alpha$  emission is that it is mixed with radiation from plasmas that are

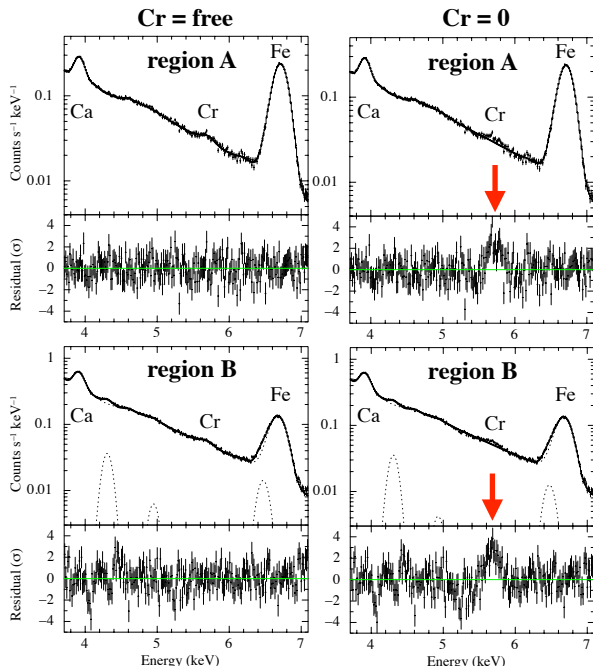


**Figure 5.** (Left row) X-ray spectra and best-fit models for region A (top) and B (bottom). (Right row) The same as the left row, but the abundances of Cr in the models are fixed at zero. At about 5.5–5.9 keV, the Cr-K $\alpha$  line emission can be seen in large residuals.

less ionized or moving away from the LoS direction than the majority of plasmas. The addition of this Gaussian model changes the estimated Cr/Fe ratio slightly (Table 3), but does not affect our interpretation in section 4.2.

#### 4. DISCUSSION

In previous sections, we investigated the kinematics and elemental compositions in the inverted ejecta layers in the southeastern region of Cas A. Our results implied that the Fe-rich ejecta (i.e., the production by the complete Si burning regime) have higher velocities and are located on the outer side of the other materials that should be produced on the inner side of the SN explosion. These would be helpful to infer the inversion process during the explosion or remnant’s evolution. In this section, we discuss these observational properties in more detail to understand the origin of the inverted layers.

##### 4.1. The kinematics of the inverted layers

In section 3.1, we found that the current velocities of the Fe-rich structures are higher than those of the Si/O-rich structures based on our proper motion measurements and the Doppler velocity measurements in Rutherford et al. (2013). On the other hand, the estima-

tions of the expansion index implied that the Si/O-rich structures seem to have undergone stronger deceleration than the Fe-rich structures. In the piston mechanism proposed in DeLaney et al. (2010), the Si/O-rich materials have higher velocities and larger radii at the beginning. Orlando et al. (2021) have demonstrated that the dense Fe-rich ejecta push out the less dense ejecta above (including Si), breaking through some of it (see also Orlando et al. 2016). Here, the low density Si/O-rich ejecta should experience strong deceleration, which may support our observations well. We here discuss the history of the expansion of each structure taking the deceleration into account.

We calculated the expansion index (see Table 2), which keeps the information of the ejecta deceleration, using the following equation:

$$m = \mu \times \frac{r}{t} \quad (1)$$

where  $m$ ,  $\mu$ ,  $r$ , and  $t$  indicate the expansion index, the observed proper motion, the distance from the explosion center, and the age of the remnant, respectively. Dividing the current velocity by the expansion index, we can obtain a free expansion velocity for traveling the current distance (shown in the 8th row of the Table 2), which would reflect the initial ejecta velocity roughly. As a result, we found that the free expansion velocities of the Fe-rich ejecta are still higher than those of the Si/O-rich ejecta.

In order to more accurately discuss the amount of deceleration, we solved for the time evolution of the supernova remnant assuming the momentum conservation law. Here, we assume that the total mass of the remnant is increased by sweeping through the surrounding medium. We then considered two cases for the density profile of the surrounding medium: a constant density and a radial dependence on the density. In the former, as the simplest case, we assume a uniform surrounding medium with the density of  $\rho_0$  as follows:

$$\frac{v}{v_0} = \frac{1}{1 + \frac{4\pi\rho_0 r_1^3}{3M_{\text{ej}}} \left(\frac{r}{r_1}\right)^3} \equiv \frac{1}{1 + A \left(\frac{r}{r_1}\right)^3} \quad (2)$$

where  $M_{\text{ej}}$ ,  $v_0$ , and  $A = \frac{4\pi\rho_0 r_1^3}{3M_{\text{ej}}}$  are the ejecta mass, the initial ejecta velocity, and the mass ratio between the swept-up ISM and the ejecta as defined in Eq. (2) when the ejecta expands to  $r_1$ , respectively. Here,  $r_1$  is introduced to let the parameters be non-dimensional and it is arbitrarily set ( $r_1 = 1$  pc is assumed throughout this paper). For example, if we set the typical parameters for Cas A as  $M_{\text{ej}} = 2 - 4M_{\odot}$  (Laming & Hwang 2003; Young et al. 2006) and  $\rho_0 = 10^{-24}$  g cm $^{-3}$ , we get  $A = 3.09 - 1.55 \times 10^{-2}$ .

**Table 3.** The best-fit parameters of spectral fittings for region A and B

Region	Model	Fe	Cr	Mass Ratio [%]	$\chi^2/\text{dof}$	$\chi^2/\text{dof}$	Significance <sup>a</sup>
				(Cr/Fe)	Cr=0	Cr=free	
A	tbabs*gsmooth*vvpschock	7.18 <sup>+0.29</sup> <sub>-0.27</sub>	3.96 <sup>+0.66</sup> <sub>-0.66</sub>	0.51 <sup>+0.11</sup> <sub>-0.10</sub>	313.08/220	234.99/219	7.91 $\sigma$
B	tbabs*gsmooth*(vvpschock + gauss $\times$ 2)	2.86 <sup>+0.02</sup> <sub>-0.05</sub>	3.82 <sup>+0.51</sup> <sub>-0.58</sub>	1.24 <sup>+0.19</sup> <sub>-0.20</sub>	496.79/214	385.42/213	7.35 $\sigma$
B	tbabs*gsmooth*(vvpschock + gauss $\times$ 3)	2.12 <sup>+0.12</sup> <sub>-0.16</sub>	3.20 <sup>+0.44</sup> <sub>-0.43</sub>	1.40 <sup>+0.32</sup> <sub>-0.25</sub>	445.78/211	297.50/210	8.27 $\sigma$

<sup>a</sup>1 $\sigma$  corresponds to a confidence interval of 68.3%.

When solving the momentum conservation law, the initial parameters required for the calculation are only the initial velocity  $v_0$  and the mass ratio  $A$ . We solved this equation to reproduce the observational properties obtained from the image analysis in the Fe-rich (Blob 1) and Si/O-rich (Blob 10) ejecta.

The left panels of Figure 6 show the time evolution of the radius, velocity, and expansion index obtained from our calculations. Here we set  $v_0 = 8200 \text{ km s}^{-1}$  and  $A = 1.16 \times 10^{-2}$  for the Fe-rich ejecta (red curve) and  $v_0 = 4440 \text{ km s}^{-1}$  and  $A = 1.17$  for the Si/O-rich ejecta (blue curve), which reproduces the observational properties well. As a result, we found that the velocity of the Si/O-rich ejecta cannot be higher than that of the Fe-rich ejecta in the entire history of the expansion, even taking into account the statistical errors. Therefore, the inversion of the ejecta kinematics seems to have been produced at a very early stage of the remnant evolution or during the explosion, although there could be a large uncertainty in the initial velocity estimations using our simple calculations.

We would note that the mass ratio  $A = 1.17$  for the Si/O-rich ejecta is almost two orders of magnitude larger than that for the Fe-rich ejecta, which implies that the Si/O-rich ejecta has encountered a denser ISM/CSM environment and/or had a lower ejecta density. Here the ejecta piston mechanism may explain this larger deceleration for the Si/O-rich ejecta (e.g., DeLaney et al. 2010; Orlando et al. 2021). In the simulations of Orlando et al. (2021), the density of Si ejecta at the outermost region in the early remnant stage have a much lower density than that of Fe ejecta (see top panels of Fig. 9 in the paper). The low-density Si ejecta undergoes a stronger slowdown and are eventually overtaken by the high-density Fe ejecta, which could be the main reason for the high mass ratio  $A$  for the Si/O-rich ejecta in this region.

We then proceed to consider the latter model as a more realistic case, which reflects an SNR evolution in the progenitor’s wind bubble. The expansion param-

eters observed in Cas A are known to be explained well with a pre-SN wind of a red supergiant, where the surrounding density profile is expressed with a function of  $\rho \propto r^{-2}$  (e.g., Chevalier & Oishi 2003). To calculate the SNR evolution in the progenitor’s wind, we define the wind density profile of  $\rho = A'r^{-2}$ . For a steady wind,  $A'$  can be written as  $A' = \dot{M}/4\pi v_w$  using the mass loss rate  $\dot{M}$  and wind speed  $v_w$  (Chevalier & Oishi 2003). In this case, Eq. (2) can be rewritten as follows:

$$\frac{v}{v_0} = \frac{1}{1 + \frac{4\pi A' r_1}{3M_{\text{ej}}} \left(\frac{r}{r_1}\right)} \equiv \frac{1}{1 + B \left(\frac{r}{r_1}\right)} \quad (3)$$

where  $B = \frac{4\pi A' r_1}{3M_{\text{ej}}}$ , and the other parameters are the same as in Eq. (2). The time evolution of the case with  $v_0 = 9280 \text{ km s}^{-1}$ ,  $B = 0.148$  (red line) and with  $v_0 = 21510 \text{ km s}^{-1}$ ,  $B = 10.2$  (blue line) is shown in the right panels of Figure 6, which reproduces well the observed results for Fe-rich and Si/O-rich ejecta, respectively. Here, assuming  $M_{\text{ej}} = 4M_{\odot}$ , the parameter  $A'$  of the equations that well represent the observed values for the Fe-rich and O-rich ejecta are  $9.12 \times 10^{13} \text{ g cm}^{-1}$  and  $6.29 \times 10^{15} \text{ g cm}^{-1}$ , respectively. The obtained values for the Fe-rich ejecta are consistent with  $1.00 \times 10^{14} \text{ g cm}^{-1}$ , the value obtained in Chevalier & Oishi (2003). This result suggests that the kinetic and spatial inversion should have occurred  $\sim 10$ – $30$  yrs after the explosion even if assuming the expansion in the power-law density profile, which would be consistent with the piston mechanism proposed by DeLaney et al. (2010); Orlando et al. (2021). Therefore, even assuming either of the two density profiles, our results support the inversion at the early stage of the remnant evolution.

#### 4.2. Constraining the burning regimes

In section 3.2, we found that the Cr/Fe mass ratio in the Fe/Si-rich region (region B) is larger than that in the Fe-rich region (region A), which implies that the complete Si burning layer is located just above the incomplete Si burning layer. In this section, we quantita-

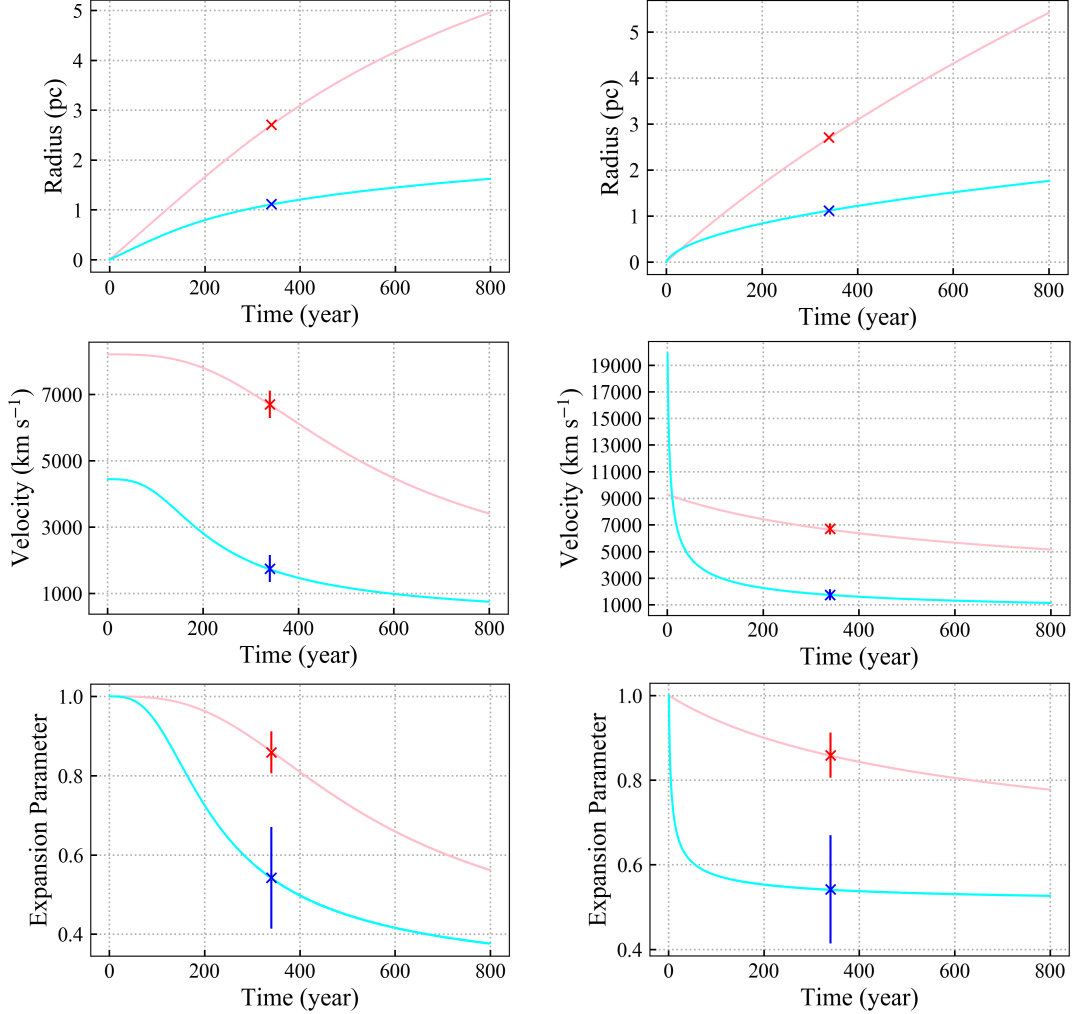


**Figure 6.** Time evolution of the radius (top panels), the velocity (middle panels), and the expansion index (bottom panels) from the momentum conservation law compared with the observed values for Blob 1 (red crosses) and Blob 10 (blue crosses). The density profiles of the surrounding medium are assumed to be uniform (left panels) and those formed by the wind of the progenitor star (right panels). Solid lines show our best-fit models for explaining the SNR parameters.

tively discuss the observed mass ratios compared with a theoretical model to understand the nucleosynthetic origin of each region.

The observed Cr/Fe mass ratio can be used for determining the peak temperature during the Si burning regime (Yamaguchi et al. 2017; Sato et al. 2020a, 2021; Ikeda et al. 2022). Figure 7 shows the relation between the peak temperature during the nuclear burning and the Cr/Fe mass ratio in a 1D SN model used in Sato et al. (2020b, 2021). Around  $T_{\text{peak}} = 5.5$  GK, there is a transition between the incomplete and complete Si burning regimes, where the Cr/Fe mass ratio shows a difference of almost one order of magnitude. As for the Fe-rich region, the observed mass ratio (red area in the figure) falls within the complete Si burning regime as already reported in Sato et al. (2021). On the other

hand, the Cr/Fe mass ratio in the Fe/Si-rich ejecta (blue area in the figure) is significantly out of the range of the complete Si burning regime, suggesting the incomplete Si burning origin ( $T_{\text{peak}} < 5.5$  GK) for this structure.

The Cr/Fe mass ratio in the Fe/Si-rich ejecta is inconsistent with the production at the complete Si burning regime, though it is lower than the typical value at the incomplete Si burning around  $T_{\text{peak}} \approx 5$  GK. One possibility is that most of the incomplete Si burning products are still not heated (e.g., Laming & Temim 2020). Another is the strong  $\alpha$ -rich freezeout. Maeda & Nomoto (2003) have shown that strong  $\alpha$ -rich freezeout realized by asymmetric explosions suppresses the production of elements produced by the incomplete Si burning regime, such as Cr and Mn.



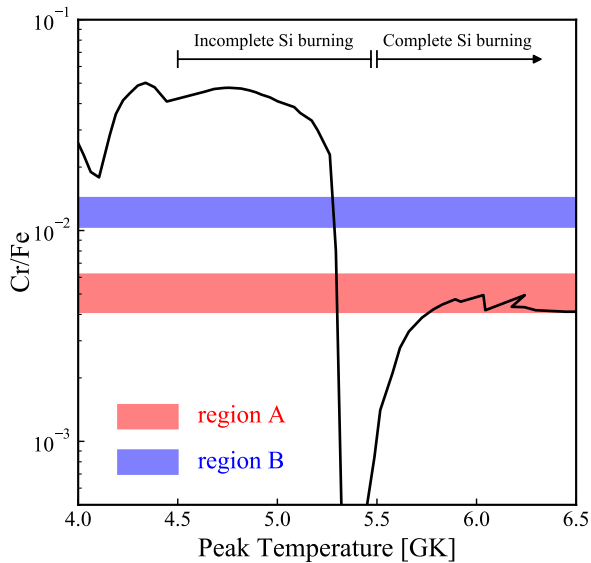


**Figure 7.** The relation between the peak temperature and the Cr/Fe mass ratio in a CC SN model. We assumed a  $15 M_{\odot}$  progenitor with sub-solar metallicity of  $Z = 0.5 Z_{\odot}$  and a high explosion energy of  $3 \times 10^{51}$  erg (see Sato et al. 2020b, 2021). The red and blue areas indicate the observational values in region A and B, respectively.

To consider the amount of contamination from the ejecta produced by the complete Si burning would allow us to discuss the low Cr/Fe ratio in region B quantitatively. In the SN model we used, the typical Cr/Fe mass ratios by the complete and incomplete Si burning are about 0.004 and 0.04, respectively. Using these values, we have roughly estimated that the contribution from the complete Si burning ejecta in this region is  $\sim 80\%$  to reproduce the observed ratio in region B. Interestingly, the contribution of the incomplete Si burning is small even in the inner Fe/Si-rich region, indicating most of Fe ( $\gtrsim 80\%$ ) in the entire east region are the complete Si burning (i.e.,  $\alpha$ -rich freeze out) origin.

The inversion of these Si burning layers would be useful to discuss the formation process of the inverted layers in the southeastern region of Cas A. Currently, the ejecta pistons during the SNR evolution would be the reasonable mechanism to explain it. On the other hand, the inversion of the adjacent Si burning layers should occur

before the inversion between Fe and Si ejecta, which may indicate the ejecta overturning during the explosion. In addition, such strong asymmetry could suppress the incomplete Si burning products (Maeda & Nomoto 2003), and this picture supports our results well. Further theoretical studies comparing with our observations will be helpful to understand the origin of the layered structure and the strong asymmetry during the SN explosion.

## 5. SUMMARY

Central strong activities are widely believed to be an important process in the explosion of massive stars. X-ray observations of the Cassiopeia A supernova remnant have indicated a possibility of “overturning” of the ejecta during the explosion, which is the best target to test such a strong asymmetry. In this paper, we have investigated the kinematic and nucleosynthetic properties of the inverted ejecta layers to understand its formation process and the SN central activity using the Chandra observations.

Based on imaging and spectral analysis, we found that the 3D velocities of Fe- and Si/O-rich ejecta are  $>4,500$  km  $s^{-1}$  and  $\sim 2,000$ – $3,000$  km  $s^{-1}$ , respectively. Even considering the deceleration, the velocity of the Si/O-rich ejecta is rarely higher than that of the Fe-rich ejecta in the entire history of the expansion.

In addition, we measured the Cr/Fe mass ratios in the ejecta layers to constrain their burning regime. We found that the mass ratio in the Fe/Si-rich region located at the inside of the Fe-rich region is significantly higher than that in the Fe-rich region. This means that the complete Si burning layer is located just outside the incomplete Si burning layer. All the results suggest that the ejecta overturning has been produced at the early stages of the remnant’s evolution or during the supernova explosion of Cassiopeia A. In the future, combined with theoretical modelings, our results will lead to an understanding of the origin of this spatial inversion of the ejecta layers.

## ACKNOWLEDGEMENTS

We thank Dr. Takashi Yoshida and Prof. Hideyuki Umeda for providing the nucleosynthesis data. This work was supported by JSPS KAKENHI Grant Numbers 18H03722, 19K14749, 20H01941, and 20K20527.

## REFERENCES

- Alarie, A., Bilodeau, A., & Drissen, L. 2014, MNRAS, 441, 2996, doi: [10.1093/mnras/stu774](https://doi.org/10.1093/mnras/stu774)
- Anders, E., & Grevesse, N. 1989, GeoCoA, 53, 197, doi: [10.1016/0016-7037\(89\)90286-X](https://doi.org/10.1016/0016-7037(89)90286-X)
- Blondin, J. M., Mezzacappa, A., & DeMarino, C. 2003, ApJ, 584, 971, doi: [10.1086/345812](https://doi.org/10.1086/345812)
- Burrows, A., Hayes, J., & Fryxell, B. A. 1995, ApJ, 450, 830, doi: [10.1086/176188](https://doi.org/10.1086/176188)

- Burrows, A., & Vartanyan, D. 2021, *Nature*, 589, 29, doi: [10.1038/s41586-020-03059-w](https://doi.org/10.1038/s41586-020-03059-w)
- Chevalier, R. A., & Oishi, J. 2003, *ApJL*, 593, L23, doi: [10.1086/377572](https://doi.org/10.1086/377572)
- DeLaney, T., Kassim, N. E., Rudnick, L., & Perley, R. A. 2014, *ApJ*, 785, 7, doi: [10.1088/0004-637X/785/1/7](https://doi.org/10.1088/0004-637X/785/1/7)
- DeLaney, T., Rudnick, L., Stage, M. D., et al. 2010, *ApJ*, 725, 2038, doi: [10.1088/0004-637X/725/2/2038](https://doi.org/10.1088/0004-637X/725/2/2038)
- Farnebäck, G. 2003, in *Scandinavian conference on Image analysis*, Springer, 363–370
- Fesen, R. A., & Milisavljevic, D. 2016, *ApJ*, 818, 17, doi: [10.3847/0004-637X/818/1/17](https://doi.org/10.3847/0004-637X/818/1/17)
- Fesen, R. A., Morse, J. A., Chevalier, R. A., et al. 2001, *AJ*, 122, 2644, doi: [10.1086/323539](https://doi.org/10.1086/323539)
- Fesen, R. A., Hammell, M. C., Morse, J., et al. 2006, *ApJ*, 636, 859, doi: [10.1086/498092](https://doi.org/10.1086/498092)
- Fryer, C. L., & Heger, A. 2000, *ApJ*, 541, 1033, doi: [10.1086/309446](https://doi.org/10.1086/309446)
- Grefenstette, B. W., Harrison, F. A., Boggs, S. E., et al. 2014, *Nature*, 506, 339, doi: [10.1038/nature12997](https://doi.org/10.1038/nature12997)
- Grefenstette, B. W., Fryer, C. L., Harrison, F. A., et al. 2017, *ApJ*, 834, 19, doi: [10.3847/1538-4357/834/1/19](https://doi.org/10.3847/1538-4357/834/1/19)
- Holland-Ashford, T., Lopez, L. A., & Auchettl, K. 2020, *ApJ*, 889, 144, doi: [10.3847/1538-4357/ab64e4](https://doi.org/10.3847/1538-4357/ab64e4)
- Holland-Ashford, T., Lopez, L. A., Auchettl, K., Temim, T., & Ramirez-Ruiz, E. 2017, *ApJ*, 844, 84, doi: [10.3847/1538-4357/aa7a5c](https://doi.org/10.3847/1538-4357/aa7a5c)
- Hughes, J. P., Rakowski, C. E., Burrows, D. N., & Slane, P. O. 2000, *ApJL*, 528, L109, doi: [10.1086/312438](https://doi.org/10.1086/312438)
- Hwang, U., Holt, S. S., & Petre, R. 2000, *ApJL*, 537, L119, doi: [10.1086/312776](https://doi.org/10.1086/312776)
- Hwang, U., & Laming, J. M. 2003, *ApJ*, 597, 362, doi: [10.1086/378269](https://doi.org/10.1086/378269)
- Hwang, U., Laming, J. M., Badenes, C., et al. 2004, *ApJL*, 615, L117, doi: [10.1086/426186](https://doi.org/10.1086/426186)
- Ikeda, T., Uchiyama, Y., Sato, T., et al. 2022, arXiv e-prints, arXiv:2201.03753. <https://arxiv.org/abs/2201.03753>
- Isensee, K., Rudnick, L., DeLaney, T., et al. 2010, *ApJ*, 725, 2059, doi: [10.1088/0004-637X/725/2/2059](https://doi.org/10.1088/0004-637X/725/2/2059)
- Isensee, K., Olmschenk, G., Rudnick, L., et al. 2012, *ApJ*, 757, 126, doi: [10.1088/0004-637X/757/2/126](https://doi.org/10.1088/0004-637X/757/2/126)
- Janka, H.-T. 2012, *Annual Review of Nuclear and Particle Science*, 62, 407, doi: [10.1146/annurev-nucl-102711-094901](https://doi.org/10.1146/annurev-nucl-102711-094901)
- Janka, H.-T., Melson, T., & Summa, A. 2016, *Annual Review of Nuclear and Particle Science*, 66, 341, doi: [10.1146/annurev-nucl-102115-044747](https://doi.org/10.1146/annurev-nucl-102115-044747)
- Janka, H. T., & Mueller, E. 1996, *A&A*, 306, 167
- Katsuda, S., Morii, M., Janka, H.-T., et al. 2018, *ApJ*, 856, 18, doi: [10.3847/1538-4357/aab092](https://doi.org/10.3847/1538-4357/aab092)
- Khokhlov, A. M., Höflich, P. A., Oran, E. S., et al. 1999, *ApJL*, 524, L107, doi: [10.1086/312305](https://doi.org/10.1086/312305)
- Laming, J. M., & Hwang, U. 2003, *ApJ*, 597, 347, doi: [10.1086/378268](https://doi.org/10.1086/378268)
- Laming, J. M., & Temim, T. 2020, *ApJ*, 904, 115, doi: [10.3847/1538-4357/abc1e5](https://doi.org/10.3847/1538-4357/abc1e5)
- Lopez, L. A., Ramirez-Ruiz, E., Castro, D., & Pearson, S. 2013, *ApJ*, 764, 50, doi: [10.1088/0004-637X/764/1/50](https://doi.org/10.1088/0004-637X/764/1/50)
- Lopez, L. A., Ramirez-Ruiz, E., Huppenkothen, D., Badenes, C., & Pooley, D. A. 2011, *ApJ*, 732, 114, doi: [10.1088/0004-637X/732/2/114](https://doi.org/10.1088/0004-637X/732/2/114)
- Maeda, K., & Nomoto, K. 2003, *ApJ*, 598, 1163, doi: [10.1086/378948](https://doi.org/10.1086/378948)
- Milisavljevic, D., & Fesen, R. A. 2013, *ApJ*, 772, 134, doi: [10.1088/0004-637X/772/2/134](https://doi.org/10.1088/0004-637X/772/2/134)
- . 2015, *Science*, 347, 526, doi: [10.1126/science.1261949](https://doi.org/10.1126/science.1261949)
- Orlando, S., Miceli, M., Pumo, M. L., & Bocchino, F. 2016, *ApJ*, 822, 22, doi: [10.3847/0004-637X/822/1/22](https://doi.org/10.3847/0004-637X/822/1/22)
- Orlando, S., Wongwathanarat, A., Janka, H. T., et al. 2021, *A&A*, 645, A66, doi: [10.1051/0004-6361/202039335](https://doi.org/10.1051/0004-6361/202039335)
- Patnaude, D. J., & Fesen, R. A. 2014, *ApJ*, 789, 138, doi: [10.1088/0004-637X/789/2/138](https://doi.org/10.1088/0004-637X/789/2/138)
- Picquenot, A., Acero, F., Holland-Ashford, T., Lopez, L. A., & Bobin, J. 2021, *A&A*, 646, A82, doi: [10.1051/0004-6361/202039170](https://doi.org/10.1051/0004-6361/202039170)
- Reed, J. E., Hester, J. J., Fabian, A. C., & Winkler, P. F. 1995, *ApJ*, 440, 706, doi: [10.1086/175308](https://doi.org/10.1086/175308)
- Rutherford, J., Dewey, D., Figueroa-Feliciano, E., et al. 2013, *ApJ*, 769, 64, doi: [10.1088/0004-637X/769/1/64](https://doi.org/10.1088/0004-637X/769/1/64)
- Sato, T., Bravo, E., Badenes, C., et al. 2020a, *ApJ*, 890, 104, doi: [10.3847/1538-4357/ab6aa2](https://doi.org/10.3847/1538-4357/ab6aa2)
- Sato, T., & Hughes, J. P. 2017, *ApJ*, 845, 167, doi: [10.3847/1538-4357/aa8305](https://doi.org/10.3847/1538-4357/aa8305)
- Sato, T., Katsuda, S., Morii, M., et al. 2018, *ApJ*, 853, 46, doi: [10.3847/1538-4357/aaa021](https://doi.org/10.3847/1538-4357/aaa021)
- Sato, T., Yoshida, T., Umeda, H., et al. 2020b, *ApJ*, 893, 49, doi: [10.3847/1538-4357/ab822a](https://doi.org/10.3847/1538-4357/ab822a)
- Sato, T., Maeda, K., Nagataki, S., et al. 2021, *Nature*, 592, 537, doi: [10.1038/s41586-021-03391-9](https://doi.org/10.1038/s41586-021-03391-9)
- Schure, K. M., Vink, J., García-Segura, G., & Achterberg, A. 2008, *ApJ*, 686, 399, doi: [10.1086/591432](https://doi.org/10.1086/591432)
- Smith, J. D. T., Rudnick, L., Delaney, T., et al. 2009, *ApJ*, 693, 713, doi: [10.1088/0004-637X/693/1/713](https://doi.org/10.1088/0004-637X/693/1/713)
- Takiwaki, T., Kotake, K., & Sato, K. 2009, *ApJ*, 691, 1360, doi: [10.1088/0004-637X/691/2/1360](https://doi.org/10.1088/0004-637X/691/2/1360)
- Takiwaki, T., Kotake, K., & Suwa, Y. 2012, *ApJ*, 749, 98, doi: [10.1088/0004-637X/749/2/98](https://doi.org/10.1088/0004-637X/749/2/98)

- Thielemann, F.-K., Nomoto, K., & Hashimoto, M.-A. 1996, ApJ, 460, 408, doi: [10.1086/176980](https://doi.org/10.1086/176980)
- Tsuchioka, T., Uchiyama, Y., Higurashi, R., et al. 2021, ApJ, 912, 131, doi: [10.3847/1538-4357/abf2bd](https://doi.org/10.3847/1538-4357/abf2bd)
- Vink, J. 2004, NewAR, 48, 61, doi: [10.1016/j.newar.2003.11.008](https://doi.org/10.1016/j.newar.2003.11.008)
- Wheeler, J. C., Maund, J. R., & Couch, S. M. 2008, ApJ, 677, 1091, doi: [10.1086/528366](https://doi.org/10.1086/528366)
- Winkler, P. F., & Petre, R. 2007, ApJ, 670, 635, doi: [10.1086/522101](https://doi.org/10.1086/522101)
- Wongwathanarat, A., Janka, H.-T., Müller, E., Pllumbi, E., & Wanajo, S. 2017, ApJ, 842, 13, doi: [10.3847/1538-4357/aa72de](https://doi.org/10.3847/1538-4357/aa72de)
- Woosley, S. E., Arnett, W. D., & Clayton, D. D. 1973, ApJS, 26, 231, doi: [10.1086/190282](https://doi.org/10.1086/190282)
- Woosley, S. E., & Weaver, T. A. 1995, ApJS, 101, 181, doi: [10.1086/192237](https://doi.org/10.1086/192237)
- Yamaguchi, H., Hughes, J. P., Badenes, C., et al. 2017, ApJ, 834, 124, doi: [10.3847/1538-4357/834/2/124](https://doi.org/10.3847/1538-4357/834/2/124)
- Young, P. A., Fryer, C. L., Hungerford, A., et al. 2006, ApJ, 640, 891, doi: [10.1086/500108](https://doi.org/10.1086/500108)